A microstructure image-based numerical model for predicting the fracture toughness of alumina trihydrate (ATH) filled poly(methyl methacrylate) (PMMA) composites

Ruoyu Zhang*, Idris K. Mohammed, Ambrose C. Taylor, Maria N. Charalambides

Imperial College London, Department of Mechanical Engineering, South Kensington Campus, London SW7 2AZ

*: Corresponding author, r.zhang13@imperial.ac.uk

Abstract

A novel finite element model is proposed here for predicting the fracture toughness using real microstructural images and accounting for several parameters that can affect the crack propagation such as filler content, particle shape, particle agglomeration and particle debonding. The damage energy prior to the catastrophic failure of the whole microstructure is taken as the energy required for crack initiation, and the fracture toughness is calculated using the concept of a critical crack size. The predictions agree well with the measured values of the critical energy release rate at 20°C as a function of both volume fraction and mean particle size. In addition, a parametric study showed that an increase in interfacial cohesive energy leads to higher fracture energies at 60°C. The proposed methodology shows great potential and can be widely applied to other particulate composites, enabling industry to cost-effectively develop tougher, hence safer and more durable, particulate composites.

Keywords

Particle-filled Composite, Finite Element Analysis, Fracture Toughness, Microstructure Analysis

1. **Introduction**

Particle-reinforced polymer composites are widely used in applications such as paints, consumer products, and automotive parts. The matrix used in particulate composites can be a thermoset, a thermoplastic or an elastomeric polymer. The particles may be ceramic, metallic or organic, and range from nanometres to millimetres in dimensions. In addition, the particles may be spherical, plate-like, rod-like or irregular in shape.

An important subset of these particulate composites uses a lightly crosslinked thermoset polymer matrix with ceramic filler particles, examples of which include adhesives, coatings, syntactic foams and encapsulants [1-4]. The material investigated in this study, alumina trihydrate (ATH) reinforced poly(methyl methacrylate) (PMMA) is a typical example. The ATH particles used have a wide size distribution and are irregular in shape. This allows the results from this study to be generalised to other systems. The wide range of sizes and irregular shape of the ATH particles means that it is a challenge to model such a composite, and especially to predict the fracture mechanisms at the microscale and their impact on the macroscopically measured critical energy release rate, G_c. In composites with high stiffness ratio between the filler and matrix, the fracture toughness and the failure locus of the composite mainly depend on the fracture toughness of the unmodified matrix material and the properties of the interface between the particles and the matrix [5, 6]. The size, shape and the distribution of the inclusions will also affect the fracture process and the measured toughness [7].

The relationship between the composite microstructure and its macroscopic fracture behaviour has attracted a great deal of attention. An increase in filler content can lead to a higher fracture toughness (G_{IC}) at low volume fractions because the particles can block the growth of the crack, causing crack arrest or deflection. These toughening mechanisms, in addition to debonding, plastic void growth and shear yielding in the matrix can greatly increase the toughness [8]. Once the filler content

reaches a critical value, any further increase tends to cause a decrease in the measured G_{IC} value [9-13]. This can be explained by the increasing stress concentration caused by the higher volume fraction of particles and the reduced volume of polymer matrix that is able to deform and absorb energy. For example, Taylor and co-workers showed that well-dispersed ceramic nanoparticles can increase the toughness of thermoset polymers [14], but highly-agglomerated particles can result in fracture energies lower than that of the unmodified matrix material [15].

Investigations concerning the effect of particle size on the fracture toughness resulted in contradictory experimental observations. In epoxy-based composites, when the size of glass particles increased from 5 µm to 60 µm, the fracture toughness increased initially and peaked at 30 µm. A further increase in the particle size caused a decrease but the fracture toughness increased again when using particles larger than 50 µm [16, 17]. Similarly, larger silica particles can lead to higher G_{IC} values [18, 19] but reductions have also been measured [19].

To predict the behaviour of particle-reinforced composites using micromechanical finite element (FE) models, the properties of the filler, matrix and interface need to be defined. To simplify the microstructure, in early work, the particle fillers were mostly treated as perfect spheres despite this not being representative of the actual shape [20, 21]. However, as the finite element models became more advanced and computational power increased, the real microstructures measured from microscopic studies could be used to obtain more accurate predictions of the mechanical behaviour [22-24]. In most of the related literature, the particles are assumed to be behaving elastically with no damage taking place. This is a reasonable assumption as the filler particles generally have a much higher strength than that of the matrix, and observation of the failure locus generally shows that the particles do not fracture.

The modelling of the interface between the particles and the matrix has attracted major attention. Spanoudakis and Young [17] showed that the fracture toughness increases as the particle to matrix adhesion is reduced, in agreement with other work [25], although they commented that the behaviour was rather complex. A potential-

based cohesive model was proposed by Hashemi et al. [20] to simulate debonding in multilayer-coated particle reinforced composites. Basaran and Gunel [12] studied the influence of interphase properties and interparticle distance on the deformation micromechanics of composites. Távara et al. [26] proposed a linear elastic brittle interface model (LEBIM) to achieve higher accuracy in predicting the interface crack phenomenon in composites. Most of these models focused on predicting the strength of composites and achieved some success. However, predicting the fracture toughness is of greater importance for particulate composites as this is a material property that is independent of the geometry used and crucial in determining the material's response in service.

For the prediction of fracture toughness of particulate composites, several models, both analytical and numerical, have been generated [6, 27-30]. However, the existing models are either difficult to use or with low accuracy due to overly simplified assumptions. One of the early attempts was performed by Kendall [30], who developed an analytical model accounting for the effect of the matrix/fille interface. Pukánszky and Maurer [31] proposed a model based on the assumption that the change in fracture properties of a composite caused by the filler/matrix interaction was proportional to the actual value of the property. Williams [28] proposed an analytical model for predicting the fracture toughness of particulate composites assuming that the plastic void growth around debonded particles is the dominant fracture mechanism. Stapountzi et al. [27] extended the application of Williams' model to composites with relative high filler content (> 35 vol.%). However, the complicated set of possibilities required in these two models make them difficult to use. Hamdia et al. [29] generated a 2D FE model to predict the fracture toughness of nanoparticle filled composite, and the authors found that at low filler content (5 vol.%), the strength and modulus of the matrix are the most significant parameters that can influence the fracture toughness of the composites.

In this study, the prediction of the fracture toughness of particulate composites using an FE model is enabled for the first time. Unlike the previously reported numerical and analytical models, the FE model proposed in this study takes into consideration possible failures in both the matrix and/or at the matrix-filler interface. In addition, using the real microstructure of the composites is expected to further improve the

accuracy of the model. An accurate model can provide a powerful tool for composites designers; it can replace or reduce numerous, expensive trial – and – error experimental approaches when investigating the fracture behaviour of composites. The aim of this work was to produce such accurate numerical micromechanical models for fracture toughness, whose input parameters will be all independently measured such that no fitting parameters will be present.

2. Materials and experimental methods

The ATH/PMMA composite materials were supplied by E.I. DuPont Nemours & Co. A summary of the particulate composite compositions used is shown in Table 1. The effects of varying the volume fraction and the particle size were investigated. Composites A, C and E were manufactured using ATH particles with the same mean diameter (15 μm) at volume fractions of 34.7 vol%, 39.4 vol% and 44.4 vol%, respectively. Composites B, C and D had the same filler content (39.4 vol%) while the mean particle diameters were 8 μm, 15 μm and 25 μm, respectively. The size distribution of these particles measured using laser light diffraction is shown in Figure 1. Examples of the microstructures of the composites obtained using SEM are shown in Figure 2.

Fracture tests on both unfilled PMMA and the particulate composites shown in Table 1 used the single edge notched bend (SENB) geometry [33]. As shown in Figure 3, the specimen dimensions were $50 \times 10 \times 5$ mm^3. A V-shaped notch of 5 mm in depth was cut into the centre of each specimen using a horizontal milling machine. A new liquid-nitrogen-cooled razor blade was tapped into the tip of each notch to introduce a sharp crack. The loading span was set at 40 mm. A compliance correction test was performed at a displacement rate of 0.1 mm/min. The fracture tests were performed in accordance with ISO 13586 [33] using an Instron 4466 universal testing machine fitted with a 5 kN load cell at a displacement rate of 1 mm/min. The load and displacement were recorded. The measured displacements were corrected for the machine compliance and indentation. At least three replicate tests were performed for each composite.

Tensile tests were performed on unfilled PMMA according to the ASTM D638-98 standard [34]. Type-I 'dog-bone' shaped specimens were machined and provided by the material supplier. The dimensions of the specimens (Figure 4) were width $W = 10$ mm, gauge length $G = 50$ mm and thickness $B = 10$ mm. The tests were performed using an Instron 3369 universal testing machine fitted with a 5 kN load cell at a displacement rate of 5 mm/min. The load and displacement were recorded and used to calculate the engineering stress and strain. At least three replicate tests were performed.

To investigate the effect of temperature on the mechanical behaviours, all the mechanical tests were performed at ambient temperature (20°C) and at 60°C in a temperature-controlled chamber. These temperatures were chosen because the ATH/PMMA composites are mainly used as surface materials in kitchen benchtops, so 20°C represents the typical room temperature while 60 °C represents the typical working temperature, i.e., when placing a hot cooking pot on a mat on the bench surface. For the 60°C tests an Instron environmental chamber was used. The test setup was left at the raised temperature for one hour prior to commencing testing. Individual samples were loaded into the test fixture and left for 25 minutes to negate any temperature fluctuations before each test. This time period was determined through the use of dummy samples and a thermocouple. At least three replicates were tested at each temperature.

3. Numerical model methodology

To investigate the relationship between the microstructure and fracture toughness of the composites, numerical simulations were performed using volume elements (VEs) derived from the SEM micrographs of the polished composite surfaces (Figure 5). Note that the smallest particles are excluded during the conversion to simplify the meshing process, so the filler content of the FE geometry is 1-2% lower than that of the SEM image. The details of the simulations will be shown in section 3.1.

3.1 Modelling geometry and boundary conditions

The commercial finite element analysis software Abaqus with the explicit solver [35] was used for all simulations. Using an edge-tracking algorithm [36], the shape and position of all the particles, which were obtained from SEM images of the polished composite surface, were imported into Abaqus [36]. The boundary of each polygon representing a particle was then offset inwards by a small distance (1 pixel) to generate the interface. A VE size of 150 μm x 90 μm and a mesh size of 0.75 μm was used for all the simulations as these were shown to achieve a good balance of prediction accuracy and computing resource consumption.

A plane strain condition was used in all simulations so that the FE predictions could be compared with the experiments. A simple uniaxial tensile strain of 5% was applied as the boundary condition to investigate the fracture toughness of the ATH/PMMA composites. A typical VE and the boundary conditions used in the simulations are shown in Figure 5. Since the actual microstructures were used, fifteen different VEs were used for each of the five composite types A - E shown in Table 1, taken from several distinct microstructural images; a total of seventy-five simulations were therefore performed. This allowed the determination of error bars on simulation results.

3.2 Damage models and material definition

Both the PMMA and ATH constituents of the composites were treated as linear elastic isotropic materials. The ATH particles are assumed to be isotropic despite their graphitic structure. This is because modelling the orientation of the ATH particles would be computationally prohibitive. In addition, due to the high strength of the particle, the failure of the composites was assumed to be primarily caused by the failure of matrix and the debonding of interface. This means that the ATH filler in this model is simplified to be an isotropic, elastic material with no damage. The failure of the matrix was modelled using a brittle cracking model, in which the crack is initiated when the principal tensile stress reaches the crack initiation stress of the brittle material [37]. In this brittle cracking model, the crack grows in a direction normal to the direction of maximum tensile principal stress at the time of crack initiation.

Though little experimental data of the crack initiation stress of PMMA is available, using the theoretical value of $E_m/20$ (E_m being the Young's modulus of PMMA) is appropriate when the material is subjected to tension according to Zhang et al.'s study [38]. For the post-crack softening of the matrix, both Mode I and Mode II softening mechanisms were considered. For the Mode I softening mechanism, the fracture toughness, G_{IC}, of PMMA derived through the experiments outlined in section 3.1, was used to describe the linear relationship between the crack opening and post-crack stress. A shear retention model was used to model the Mode II softening, in which the post-crack shear modulus, μ_m^{cr}, is defined as a function of the crack opening displacement:

$$\mu_m^{cr} = \rho \mu_m \tag{1}$$

where μ_m is the shear modulus of uncracked matrix and ρ is the traditional shear retention factor dependent on the normal strain across the crack, e^{cr}:

$$\rho = \left(1 - \frac{e^{cr}}{e_{max}^{cr}}\right)^P \tag{2}$$

where P and e_{max}^{cr} are material parameters, which were chosen as 1 for simplicity and 1% as a typical value for the failure strain of PMMA [39] respectively.

The debonding along the filler/matrix interface was modelled using a bilinear traction-separation law (as shown in Figure 6), in which the same cohesive zone properties were assumed for both mode I and II whereas the mixed mode failure locus was taken to be linear. The values of all material parameters, i.e., interfacial linear modulus, k_σ, interfacial cohesive strength, σ_{max}^{int} and interfacial cohesive energy, γ_{int} required as input to the models are presented in the following section.

4. Results and discussion

4.1 Experimental results

The material properties of unfilled PMMA, the ATH particles and their interface obtained from literature or mechanical tests from this study (tensile and SENB tests described in section 2) are summarised in Table 2. The ATH/PMMA interface properties at 20°C were obtained using digital image correlation (DIC) during the SENB tests according to a method developed by Tan et al. [40]. However, since the camera could not be used at high temperature without causing damage to the CMOS sensor of the camera, it was not possible to obtain the interfacial properties at 60°C. Therefore, a parametric study was performed for the simulation at 60°C as will be discussed in section 4.3

The effects of volume fraction and mean particle size on the fracture toughness of the ATH/PMMA composites are shown in Figure 7 and Figure 8, respectively for the two temperatures of 20 °C and 60 °C. As expected, the standard deviations of the SENB tests are relatively large (10%- 15%). As the test temperature increased, the fracture toughness of the composites increased as shown in both figures. For example, for composite A in Table 1, a fracture toughness of 503 N/m was measured at 20°C, which increased to 541 N/m at 60°C. In contrast, the fracture toughness of the unfilled PMMA decreased from 395 N/m to 302 N/m when the test temperature increased from 20°C to 60°C, as shown in Table 2. Similar trends for the composites and unfilled PMMA have been observed by Stapountzi et al. [27]. Since the mechanical properties of the ATH fillers are barely affected by the change of temperature, the increase in the fracture toughness of ATH/PMMA composites at higher temperature indicates a higher debonding energy of the filler /matrix interface. For tests at both 20°C and 60°C, the fracture toughness of the ATH/PMMA composites decreased as the volume fraction of ATH increased, see Figure 7. A fracture toughness of 503 N/m was measured at 20°C for a volume fraction of 34.7 %, compared with 345 N/m for a volume fraction of 44.4 %. When the ATH particle mean size increased, while the volume fraction remained constant, the fracture toughness increased (see Figure 8). A fracture toughness of 305 N/m was

measured at 20°C for the composite with a mean ATH particle size of 8 µm, compared with 440 N/m for a mean particle size of 25 µm.

4.2 Estimation of composite fracture toughness using FEA models

The effect of the VE size and mesh density on the model output was first investigated. Simulations using three different VE sizes (200 μm x 120 μm, 150 μm x 90 μm and 100 μm x 60 μm) and three different mesh sizes (3 μm, 1.5 μm and 0.75 μm) were performed on Composite C in Table 1 and the predicted fracture toughness from these models was compared. The method for outputting the values of G IC from the models is described below.

To predict the fracture energy, G_{IC}, of the ATH/PMMA composite, the critical value of the damage energy, E_D, of each VE and the critical flaw size needs to be obtained. Critical damage energy is the damage energy prior to the fast crack growth. Typical energy curves obtained from the FE simulation are shown in Figure 9 and Figure 10. The recoverable elastic energy represents the energy dissipated by elastic strain, while the damage energy represents the energy dissipated through all types of damage including interfacial debonding and matrix damage. The initiation of the fast crack growth is marked by the sudden drop of the recoverable elastic energy. If the crack growth is not arrested by particles, there will be only one peak in the recoverable elastic energy curve (as is the case shown in Figure 9), while there will be multiple peaks of recoverable elastic energy if the crack growth progress is arrested as shown in the case in Figure 10. Therefore, the growth of the crack can be divided into two different types according to whether or not the crack growth is arrested by a particle (see Figure 11). By comparing Figure 9 and Figure 10, it can be concluded that crack arrest can lead to a higher critical damage energy (damage energy prior to the fast crack growth, 0.02 μJ vs. 0.035 μJ) because the crack splits and the generation of another damage zone at the new crack tip requires extra energy.

In addition, premature failure of the composites caused by the agglomeration of smaller particles (see Figure 11c) leading to matrix fracture can lead to lower critical damage energy (results not shown, this case led to Energy versus applied strain

plots similar in shape to that shown in Figure 8, i.e., with a single energy peak marking the onset of fast crack growth).

The fracture energy, G_{IC}, of the composites can be estimated from the critical damage energy output from the FE simulations (e.g., Figures 9 and 10), E_D, using:

$$G_{IC} = E_D/c \tag{3}$$

where c is the critical flaw size: the size of crack in a structure that causes failure at a particular stress level. In a brittle material, crack propagation occurs catastrophically if the crack size is above the critical size. In the simulations, the crack propagation can only be constrained by the particles, so the critical flaw size, c, was assumed to be equal to:

$$c = L_{RVE} \times \phi_f \tag{4}$$

where L_{RVE} is the length of the VE along the crack propagation direction (150 μm in Figure 4), and ϕ_f is the filler volume fraction.

Figure 12 shows one set of three VEs of different sizes. To ensure the FE predictions are comparable, the VEs share the same left bottom corner. This procedure was performed on fifteen sets of VEs taken from distinct microstructural images of the same composite, to enable a statistical analysis of the predicted fracture toughness data. The results are summarised in Table 3. It shows that if the VE size is too small (i.e.,100 μm x 60 μm), the simulation will not be able to represent the composite well and the prediction for G_{IC} would be associated with a high standard deviation (>30%) as well as a mean significantly higher than the values corresponding to the larger models (i.e., 200 μm x 120 μm and 150 μm x 90 μm). As the VE size increases, the standard deviation of the predicted fracture toughness is seen to decrease and the average values of the fifteen simulations are seen to converge to similar values. This indicates that larger VEs could lead to more

accurate fracture toughness predictions. However, it is worth to note here that larger VEs would require more computing power (40 core-hours for 200 μm x 120 μm vs. 25 core-hours for 150 μm x 90 μm). Therefore, the size of 150 μm x 90 μm was selected for the rest of the study.

On the other hand, simulations with different mesh sizes (3 μm, 1.5 μm and 0.75 μm) were performed on a 150 μm x 90 μm VE of Composite C in Table 1. As shown in Table 4, the change in mesh size showed very little effect on the predicted fracture toughness. The difference in the predicted fracture toughness obtained from the same geometry with different mesh size is almost negligible. This is somehow expected because the mesh size only affects the post-failure behaviour [38]. However, a finer mesh is recommended to get better prediction of the crack path [38]. Therefore the mesh size of 0.75 mm was selected for the rest of the study, even though this requires a higher computational power than the larger mesh sizes.

4.3 Fracture toughness model prediction at 20°C

The critical damage energies obtained from the fifteen simulations performed on each type of composite are summarised in Figure 13 and Figure 14. It shows that the change in the filler content had little effect on the value of critical damage energy (see Figure 13), and higher filler contents lead to higher critical energy (see Figure 14). This can be well explained by the crack arrest and matrix failure-initiated crack mechanisms.

For the fifteen simulations performed per composite, the frequency of the crack arrest and matrix failure-initiated crack occurring in each composite are summarised in Table 5. It shows that the change in filler content (Composites A, C and E, see Table 1) had little effect on the frequency of either of the two mechanisms, hence the change in the filler content had little impact on the value of critical damage energy (see Figure 13). Meanwhile, as particle size increased (Composites B, C and D, see Table 1), the frequency of agglomeration-induced cracks became lower while the frequency of crack arrest became higher. This well explains why Composite B has the lowest critical damage energy in Figure 14.

The FE predictions of the fracture toughness are compared to the experimental results in Figure 15 for different filler contents and in Figure 16 for different mean particle size. A good agreement is observed in all cases, with a small underestimation (5%-15%) of the average G_{IC} values when compared to the experimental data, which could result from the loss of the smaller particles during the image to VE conversion process. A more detailed statistical analysis follows below. However, it worth noting here that the error bars for the fracture toughness are equally large in experimental data as in the FE model predictions. This therefore suggests that the observed experimental variation in G_{IC} is due to a genuine variability in the complex microstructure of the composite material.

The correlation between the FE predictions and the experimental results is evaluated using the Pearson correlation coefficient, r, which is the covariance of the two variables divided by the product of their standard deviations:

$$r = \frac{\sum(x - \bar{x})(y - \bar{y})}{\sqrt{\sum(x - \bar{x})^2(y - \bar{y})^2}} \tag{5}$$

where x and y are the mean values of the experimental results and FE predictions, respectively. The values of r are 0.999 and 0.997 in fracture toughness vs filler volume fraction and mean particle size, respectively. This means the FE model gave a good prediction of the trends in fracture toughness with both filler content and particle size.

As shown in Figure 15 and Figure 16, the standard deviation in both the experimental results and the FE predictions are quite large due to the wide size distribution and irregular shapes of the particles. Therefore, a 2-tail t-statistic analysis was performed to evaluate the probability of two different sets of data being from populations with the same mean. To perform the t-statistic analysis, the value of the t-score, t, and the degree of freedom, v, need to be calculated. The t-score can be calculated from:

$$t = \frac{(\bar{a} - \bar{b})}{\sqrt{\dfrac{s_1^2}{n_1} + \dfrac{s_2^2}{n_2}}} \tag{6}$$

where $\bar{a}$ and $\bar{b}$ are the average values of the two sets of data, s_1 and s_2 are the standard deviations, and n_1 and n_2 are the number of the replicates. Because the data sets used in this study have different standard deviations, the degree of freedom can be calculated from:

$$v = \frac{\left(\dfrac{s_1^2}{n_1} + \dfrac{s_2^2}{n_2}\right)^2}{\dfrac{\left(\dfrac{s_1^2}{n_1}\right)^2}{n_1 - 1} + \dfrac{\left(\dfrac{s_2^2}{n_2}\right)^2}{n_2 - 1}} \tag{7}$$

Once the values of t and v are obtained, the probability can be found in the Critical Values table of Student's T-distribution [43]. The results from this statistical test showed that the probability of any overlapping datasets is less than 5%, which means that the trends obtained in both fracture toughness vs filler volume fraction and fracture toughness vs mean particle size are valid.

4.4 A parametric study for investigating the Fracture toughness at 60°C

As discussed in section 4.1, the interfacial properties at 20°C were obtained using DIC, which can derive the strain fields local to the crack tip of compact tension fracture experiments [38]. However, using the high-speed camera for tests where the sample is inside an environmental chamber at 60°C requires more complex experimental procedures. Therefore, a parametric modelling study was performed on the interfacial traction-separation parameters to investigate their effects on the composite's fracture toughness. The effect of changes in three parameters were considered, namely the interfacial linear modulus, k_σ, interfacial cohesive strength, σ_{max}^{int}, and interfacial cohesive energy, γ_{int} (see Figure 6). Table 6 shows the values used for these three parameters in the interfacial traction-separation law. The values were chosen to investigate the effect of these parameters on the fracture toughness prediction when they decreased, increased slightly and increased significantly from

the parameter values shown in Table 2, i.e., k_σ=3.61 GPa/µm, σ_{max}^{int} = 119 MPa and γ_{int} = 430 N/m/.

The results of the parametric studies on k_σ, σ_{max}^{int} and γ_{int},are shown in Figure 17, Figure 18 and Figure 19 respectively. The change in the interfacial linear modulus, k_σ, shows little effect on the predicted fracture toughness, see Figure 17. This agrees with several previous studies [22, 38], that as long as the value of k_σ is in a reasonable range, i.e., not too low so it introduces artificial compliance nor too high so that it causes convergence problems, it has no significant effect on the simulation results.

Increasing the cohesive strength, σ_{max}^{int}, can lead to a higher fracture toughness, but this enhancing effect peaked at 200 MPa with further increases giving no significant effect, see Figure 18. Stronger interfacial cohesion can postpone the debonding process so more energy can be dissipated before catastrophic failure. However, if the interface is much stronger than the matrix, the failure of the matrix will become the primary cause of the crack initiation, i.e., as σ_{max}^{int} increased from 100 MPa to 300 MPa, the matrix failure induced crack initiation increased from 2 out of 15 to 11 out of 15 in composite D, so the fracture toughness could not be further enhanced.

In contrast, the increase in the interfacial cohesive energy, γ_{int}, leads to a significant increase in the fracture toughness of the composites at 60°C, see Figure 19. Debonding of particles is the dominant crack initiation mechanism [44], so it is expected that the interfacial cohesive energy will have a significant effect on the fracture toughness of the composites. When γ_{int} = 600 N/m, which is approximately 40% higher than the experimentally obtained value of 430 N/m at 20°C, a very good prediction of the fracture toughness of the ATH/PMMA composites at 60°C is obtained, see Figure 19. The increase in interfacial cohesive energy, γ_{int}, at higher temperature is reasonable as higher temperatures improve the flexibility of the polymeric chains so the matrix can wet the filler surface better [45].

The new modelling methodology presented here is simple and gives accurate predictions for the fracture toughness of particulate composites. This is a significant breakthrough as there are several parameters which affect the fracture toughness

and it is impossible to quantify these effects through experiments alone or closed form analytical solutions. The models give a real insight on what drives crack initiation and growth, distinguishing between the various possible fracture mechanisms, i.e., interface debonding, matrix cracks and crack arrest at larger particles. The accuracy of the predictions is significant, given the variability and complexity of the composites at the microstructural level.

5. Conclusions

A novel approach to determine the fracture toughness of particle filled polymeric composites based on FE models is proposed. This simple methodology shows a great potential as evidenced from its validation against experimental data. The material investigated in this study is alumina trihydrate (ATH) filled poly(methyl methacrylate) (PMMA), but the method could be widely applicable. By using VEs converted from microscopic images of the real microstructure, the model takes into consideration many factors that can affect the crack progress, such as the shape and size distribution of the particles. The model was able to predict the effect of the crack arrest caused by large particles and the agglomeration of small particles leading to matrix cracking. For example, smaller particles lead to a lower probability of crack arresting and a higher probability of agglomeration-induced matrix cracks. Both of these effects lead to a lower fracture toughness. In the model, the damage energy prior to the catastrophic failure of the whole microstructure is taken as the energy required for crack initiation. In addition, since particle debonding is the dominant crack initiation mechanism [44], the critical crack size is assumed to be equal to the cross-section multiplied by the particle volume fraction. By dividing the crack initiation energy by the critical crack size, the model was able to give good predictions of the fracture toughness at 20°C. In addition, by performing a parametric study, the modelling results indicate that an increase in interfacial cohesive energy by 40% was potentially responsible for the higher fracture toughness of the composites measured at 60°C. The parametric study also shows that increasing the interfacial fracture energy is the most effective way to improve the fracture toughness of particle-filled composite. The proposed model provides significant and powerful new tools for industrial development and design of novel particle-filled composites, tailored to fit the demands of particular applications.

Acknowledgements

References

[1] Hagan EW, Charalambides MN, Young CR, Learner TJ, Hackney S. Influence of the inorganic phase concentration and geometry on the viscoelastic properties of latex coatings through the glass-transition. Polymer. 2011;52(7):1662-73.

[2] Wong C, Bollampally RS. Thermal conductivity, elastic modulus, and coefficient of thermal expansion of polymer composites filled with ceramic particles for electronic packaging. Journal of applied polymer science. 1999;74(14):3396-403.

[3] He S, Carolan D, Fergusson A, Taylor AC. Toughening epoxy syntactic foams with milled carbon fibres: Mechanical properties and toughening mechanisms. Materials & Design. 2019;169:107654.

[4] Lim YJ, Carolan D, Taylor AC. Simultaneously tough and conductive rubber–graphene–epoxy nanocomposites. Journal of Materials Science. 2016;51(18):8631-44.

[5] Fu S-Y, Feng X-Q, Lauke B, Mai Y-W. Effects of particle size, particle/matrix interface adhesion and particle loading on mechanical properties of particulate–polymer composites. Composites Part B: Engineering. 2008;39(6):933-61.

[6] Lauke B, Fu S-Y. Aspects of fracture toughness modelling of particle filled polymer composites. Composites Part B: Engineering. 2013;45(1):1569-74.

[7] Alavi F, Behravesh A, Mirzaei M. In-situ observation of fracture mechanism of wood–plastic composites in tension. Composite Interfaces. 2013;20(3):211-20.

[8] Hsieh T, Kinloch A, Masania K, Taylor A, Sprenger S. The mechanisms and mechanics of the toughening of epoxy polymers modified with silica nanoparticles. Polymer. 2010;51(26):6284-94.

[9] Evans A, Williams S, Beaumont P. On the toughness of particulate filled polymers. Journal of Materials Science. 1985;20(10):3668-74.

[10] Hussain M, Nakahira A, Nishijima S, Niihara K. Fracture behavior and fracture toughness of particulate filled epoxy composites. Materials Letters. 1996;27(1-2):21-5.

[11] Moloney AC, Kausch HH, Stieger HR. The fracture of particulate-filled epoxide resins. Journal of Materials Science. 1984;19(4):1125-30.

[12] Gunel E, Basaran C. Influence of volume fraction and interphase properties on large deformation micromechanics of particle filled acrylics. Mechanics of Materials. 2013;57:134-46.

[13] Stapountzi OA, Charalambides MN, Williams JG. Micromechanical models for stiffness prediction of alumina trihydrate (ATH)

reinforced poly (methyl methacrylate) (PMMA): Effect of filler volume fraction

and temperature. Composites Science and Technology. 2009;69:2015-23.

[14] Johnsen BB, Kinloch AJ, Mohammed RD, Taylor AC, Sprenger S. Toughening mechanisms of nanoparticle-modified epoxy polymers. Polymer. 2007;48(2):530-41.

[15] Kinloch AJ, Taylor AC. The toughening of cyanate-ester polymers Part I Physical modification using particles, fibres and woven-mats. Journal of Materials Science. 2002;37(3):433-60.

[16] Spanoudakis J, Young R. Crack propagation in a glass particle-filled epoxy resin, Part I. Journal of Materials Science. 1984;19(2):473-86.

[17] Spanoudakis J, Young RJ. Crack propagation in a glass particle-filled epoxy resin, Part II. Journal of Materials Science. 1984;19(2):487-96.

[18] Nakamura Y, Yamaguchi M, Kitayama A, Okubo M, Matsumoto T. Effect of particle size on fracture toughness of epoxy resin filled with angular-shaped silica. Polymer. 1991;32(12):2221-9.

[19] Bray D, Dittanet P, Guild F, Kinloch A, Masania K, Pearson R, et al. The modelling of the toughening of epoxy polymers via silica nanoparticles: The effects of volume fraction and particle size. Polymer. 2013;54(26):7022-32.

[20] Hashemi R, Spring DW, Paulino GH. On small deformation interfacial debonding in composite materials containing multi-coated particles. Journal of Composite Materials. 2015;49(27):3439-55.

[21] Qu M, Deng F, Kalkhoran SM, Gouldstone A, Robisson A, Van Vliet KJ. Nanoscale visualization and multiscale mechanical implications of bound rubber interphases in rubber–carbon black nanocomposites. Soft Matter. 2011;7(3):1066-77.

[22] Arora H, Tarleton E, Li-Mayer J, Charalambides M, Lewis D. Modelling the damage and deformation process in a plastic bonded explosive microstructure under tension using the finite element method. Computational Materials Science. 2015;110:91-101.

[23] Tarleton E, Charalambides M, Leppard C, Yeoh J. Micromechanical modelling of alumina trihydrate filled poly (methyl methacrylate) composites. International Journal of Materials and Structural Integrity. 2013;7(1-3):31-47.

[24] Mcwilliams B, Sano T, Yu J, Gordon A, Yen C. Influence of hot rolling on the deformation behavior of particle reinforced aluminum metal matrix composite. Materials Science and Engineering: A. 2013;577:54-63.

[25] Broutman L, Sahu S. The effect of interfacial bonding on the toughness of glass filled polymers. Materials Science and Engineering. 1971;8(2):98-107.

[26] Távara L, Moreno L, Paloma E, Mantič V. Accurate modelling of instabilities caused by multi-site interface-crack onset and propagation in composites using the sequentially linear analysis and Abaqus. Composite Structures. 2019;225:110993.

[27] Stapountzi OA, Charalambides MN, Williams JG. The Fracture Toughness of a Highly Filled Polymer Composite. In: Kounadis AN, Gdoutos EE, editors. Recent Advances in Mechanics: Selected Papers from the Symposium on Recent Advances in Mechanics, Academy of Athens, Athens, Greece, 17-19 September, 2009, Organised by the Pericles S Theocaris Foundation in Honour of PS Theocaris, on the Tenth Anniversary of His Death. Dordrecht: Springer Netherlands; 2011. p. 447-59.

[28] Williams J. Particle toughening of polymers by plastic void growth. Composites science and technology. 2010;70(6):885-91.

[29] Hamdia KM, Silani M, Zhuang X, He P, Rabczuk T. Stochastic analysis of the fracture toughness of polymeric nanoparticle composites using polynomial chaos expansions. International Journal of Fracture. 2017;206(2):215-27.

[30] Kendall K. Fracture of particulate filled polymers. British Polymer Journal. 1978;10(1):35-8.

[31] Pukánszky B, Maurer FHJ. Composition dependence of the fracture toughness of heterogeneous polymer systems. Polymer. 1995;36(8):1617-25.

[32] (Inc.) EIDNC. Safety data sheet. 2014.

[33] Plastics - Determination of fracture toughness (K_{IC} and G_{IC}) - Linear elastic fracture mechanics (LEFM) approach. Geneva: International Organization for Standardization; 2000.

[34] Standard Test Method for Tensile Properties of Plastics. Annual Book of ASTM Standard. West Conshohocken: American Society for Testing and Materials; 1998.

[35] Abaqus. 6.14 ed. Vélizy-Villacoublay, France: Dassault Systèmes.

[36] Tarleton E, Charalambides M, Leppard C. Image-based modelling of binary composites. Computational Materials Science. 2012;64:183-6.

[37] A cracking model for concrete and other brittle materials. Abaqus Analysis User's Guide. Abaqus 6.14 ed. Vélizy-Villacoublay, France: Dassault Systèmes.

[38] Zhang R, Li-Mayer J, Charalambides M. Development of an image-based numerical model for predicting the microstructure–property relationship in alumina trihydrate (ATH) filled poly (methyl methacrylate)(PMMA). International Journal of Fracture. 2018;211(1-2):125-48.

[39] Kaplan WA. Modern Plastics Encyclopedia'99: Mc Graw-Hill/Le Quinio; 1999.

[40] Tan H, Huang Y, Liu C, Geubelle PH. The Mori–Tanaka method for composite materials with nonlinear interface debonding. International Journal of Plasticity. 2005;21(10):1890-918.

[41] O. A. Stapountzi. Stiffness and fracture properties of alumina trihydrate filled poly (methyl Methacrylate) composites: Imperial College London; 2008.

[42] Jung G-D, Youn S-K, Kim B-K. Development of a three-dimensional nonlinear viscoelastic constitutive model of solid propellant. Journal of the Brazilian Society of Mechanical Sciences. 2000;22:457-76.

[43] Beyer WH. Handbook of tables for probability and statistics: Crc Press; 2019.

[44] Tsui C, Chen D, Tang C, Uskokovic P, Fan J, Xie X. Prediction for debonding damage process and effective elastic properties of glass-bead-filled modified polyphenylene oxide. Composites science and technology. 2006;66(11-12):1521-31.

[45] Sankarasubramanian S, Cruz J, Yazzie K, Sundar V, Subramanian V, Alazar T, et al. High-Temperature Interfacial Adhesion Strength Measurement in Electronic Packaging Using the Double Cantilever Beam Method. Journal of Electronic Packaging. 2017;139(2).
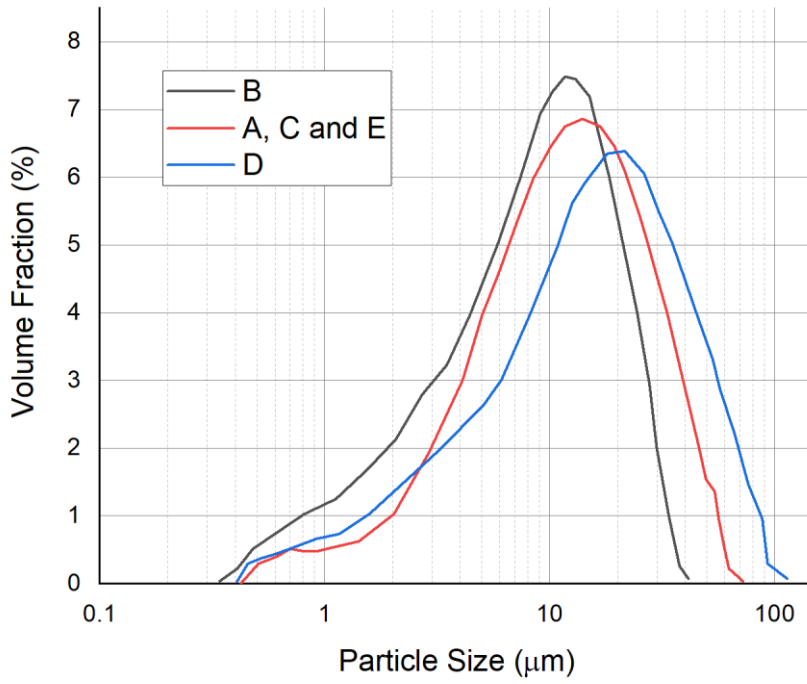
Figure 1 ATH particle size distribution obtained using the laser light scattering technique, expressed using volume fraction. The mean particle sizes used in composites B, A/C/E, and D are 8 μm, 15 μm and 25 μm, respectively.
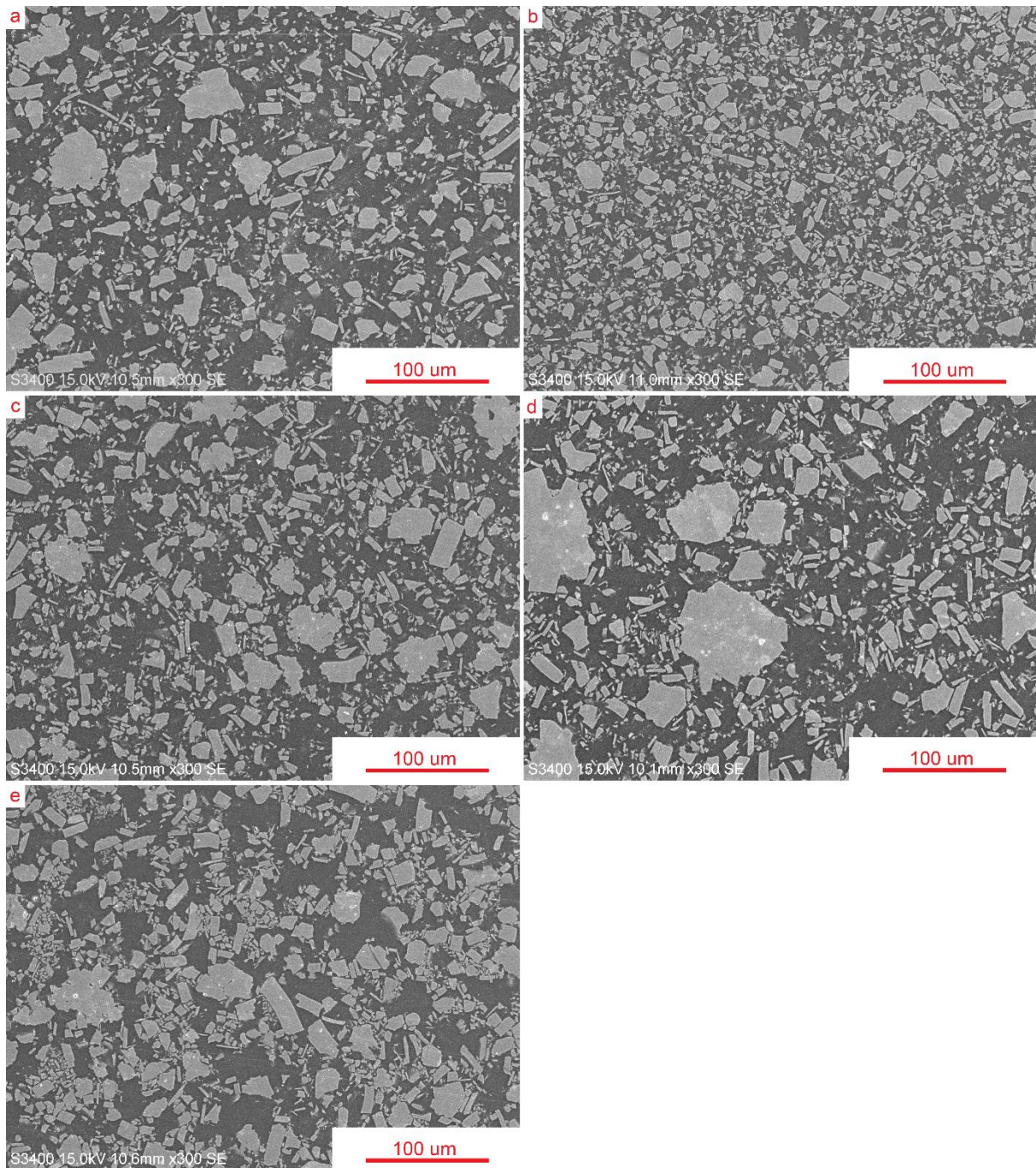
Figure 2 SEM images (x300) of polished surfaces of Composites a) Composite A with average particle size of 15 µm and volume fraction 34.7%, b) Composite B with average particle size of 8 µm and volume fraction39.4%, c) Composite C with average particle size 15 µm and volume fraction 39.4%, d) Composite D with average particle size of 25 µm and volume fraction 39.4%, and e) Composite E with average particle size 15 µm and volume fraction 44.4%.
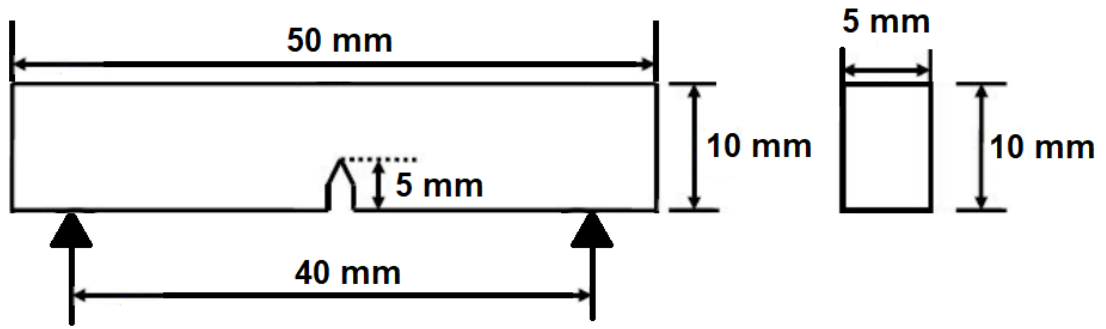
Figure 3 The dimension of the specimen used in SENB test.
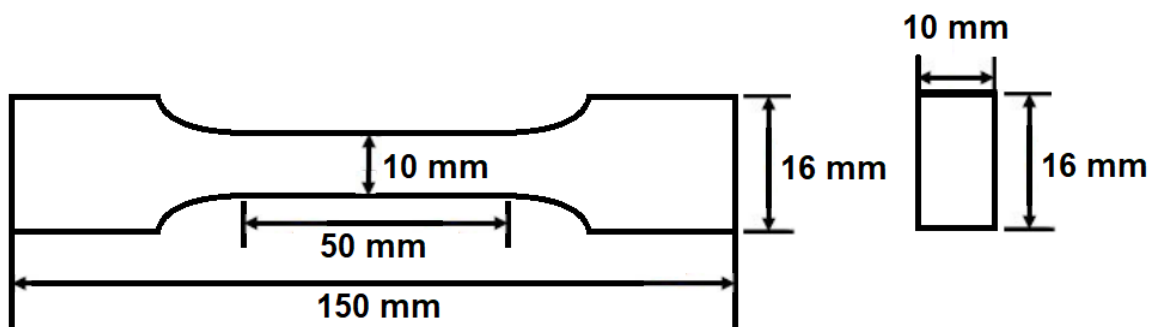
Figure 4 The dimension of the specimen used in tensile test.
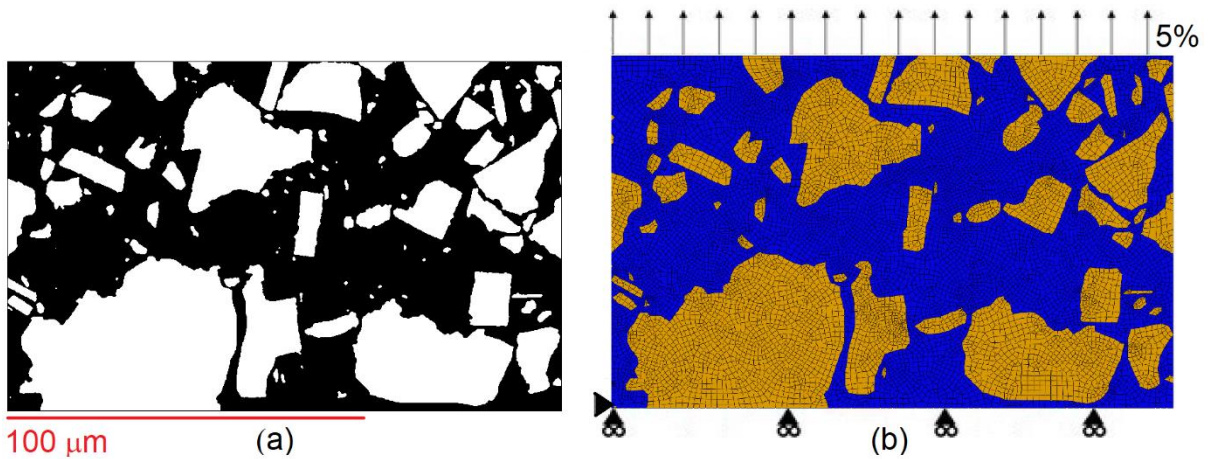
Figure 5. (a) Typical binary image converted from SEM image of the polished composite (Composite D in Table 1) surface, and (b) corresponding VE and boundary conditions.
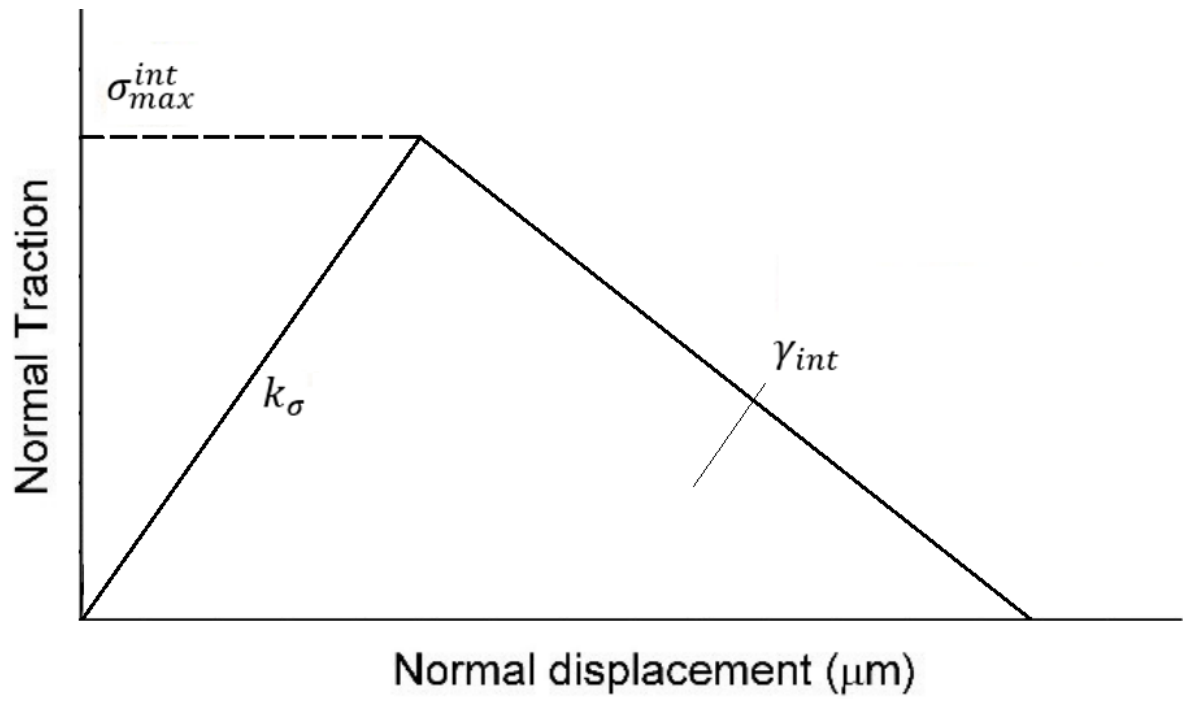
Figure 6 A typical traction-separation response for cohesive elements.
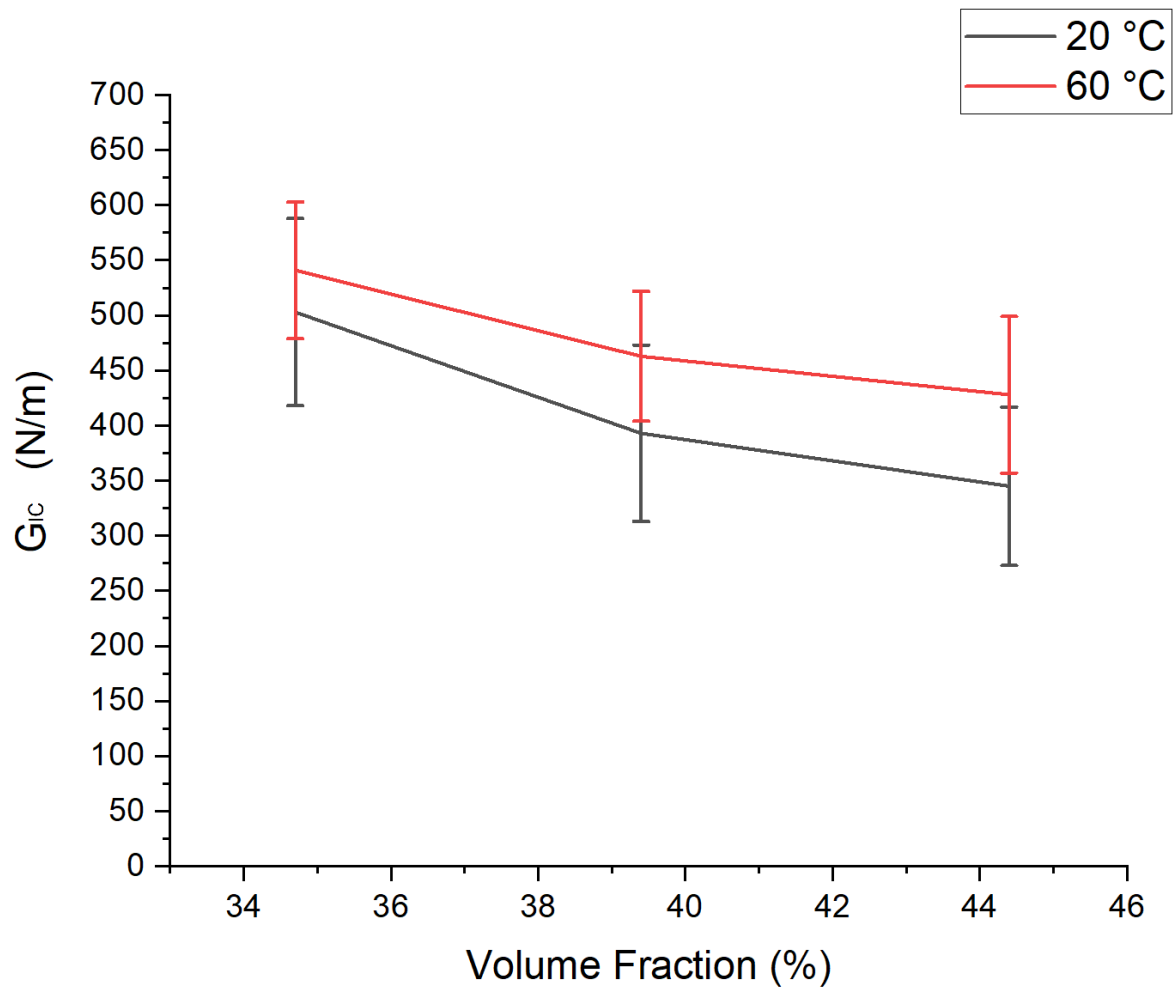
Figure 7. Effect of filler volume fraction on the fracture toughness of ATH/PMMA composites (Composites A, C and E in Table 1) at 20°C and 60°C. As volume fraction increases, the fracture toughness of the composites decreased, whilst temperature led to an increase in fracture toughness.
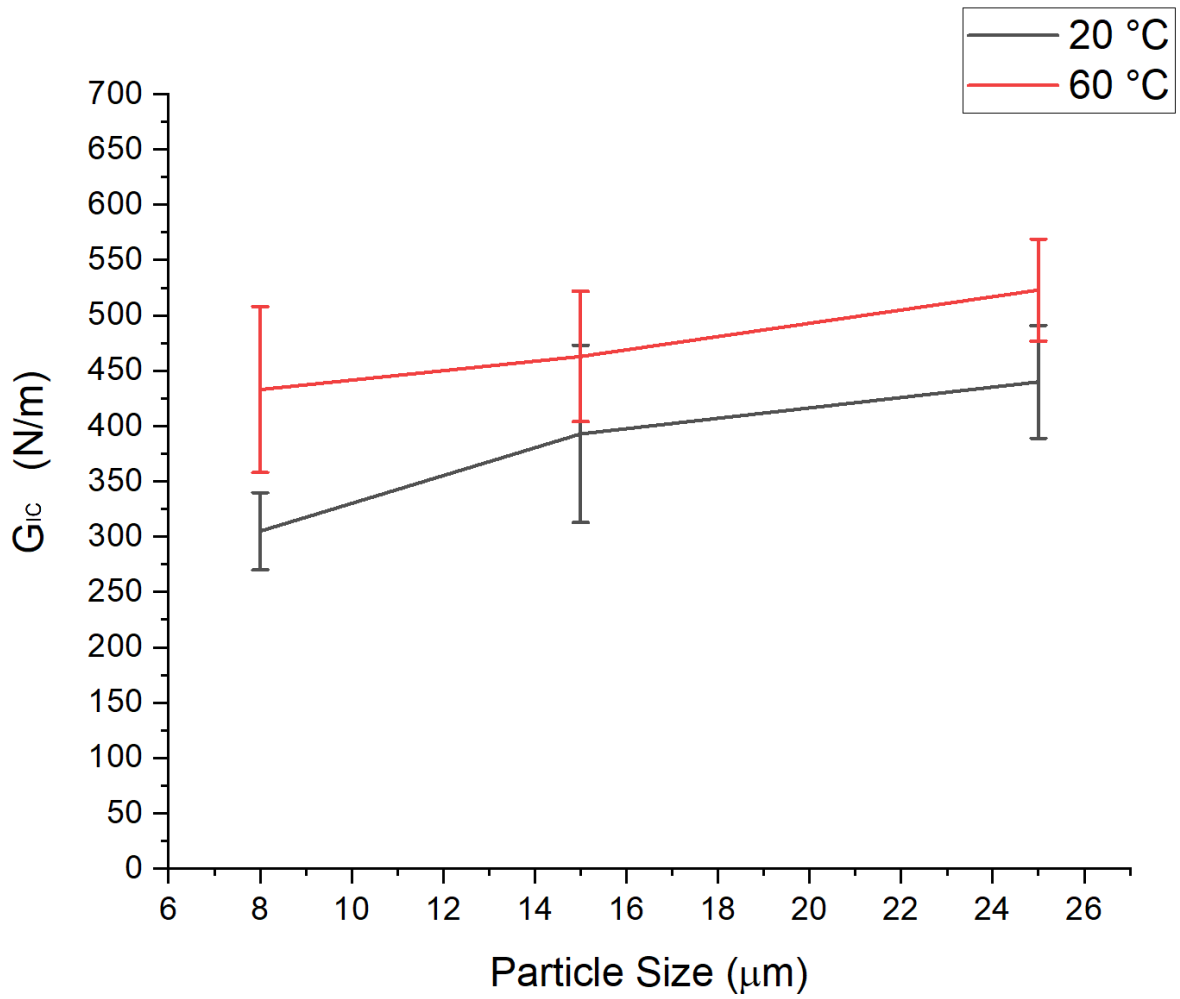
Figure 8. Effect of mean particle diameter on the fracture toughness of ATH/PMMA composites (Composites B, C and D in Table 1) at 20°C and 60°C. The fracture toughness of the composites increased while using larger particles and higher temperature.
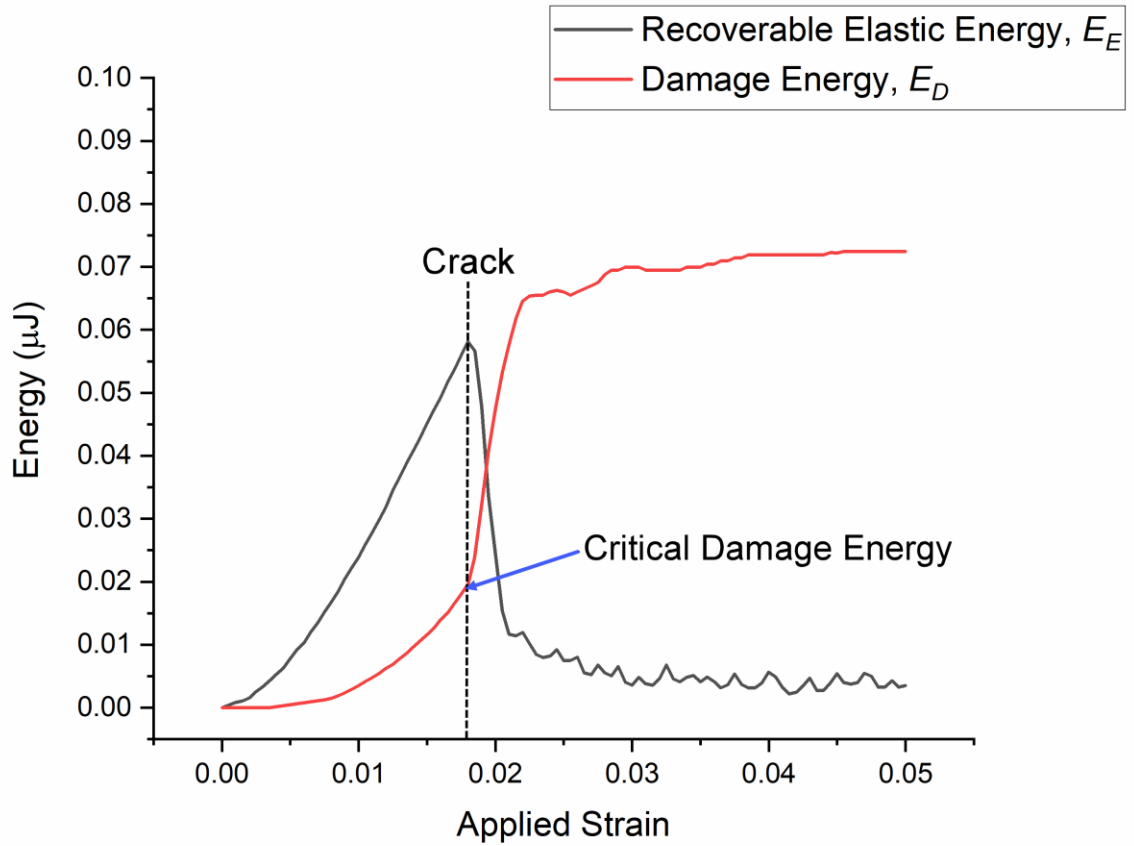
Figure 9. The recoverable elastic energy and damage energy plotted against applied strain in model cases without crack arrest (Composite B in Table 1, VE size:150 μm x 90 μm, mesh size: 0.75 μm). Damage energy increases as the strain increases with no crack growth arrest. The drop in the recoverable elastic energy marks the onset of the fast crack growth.
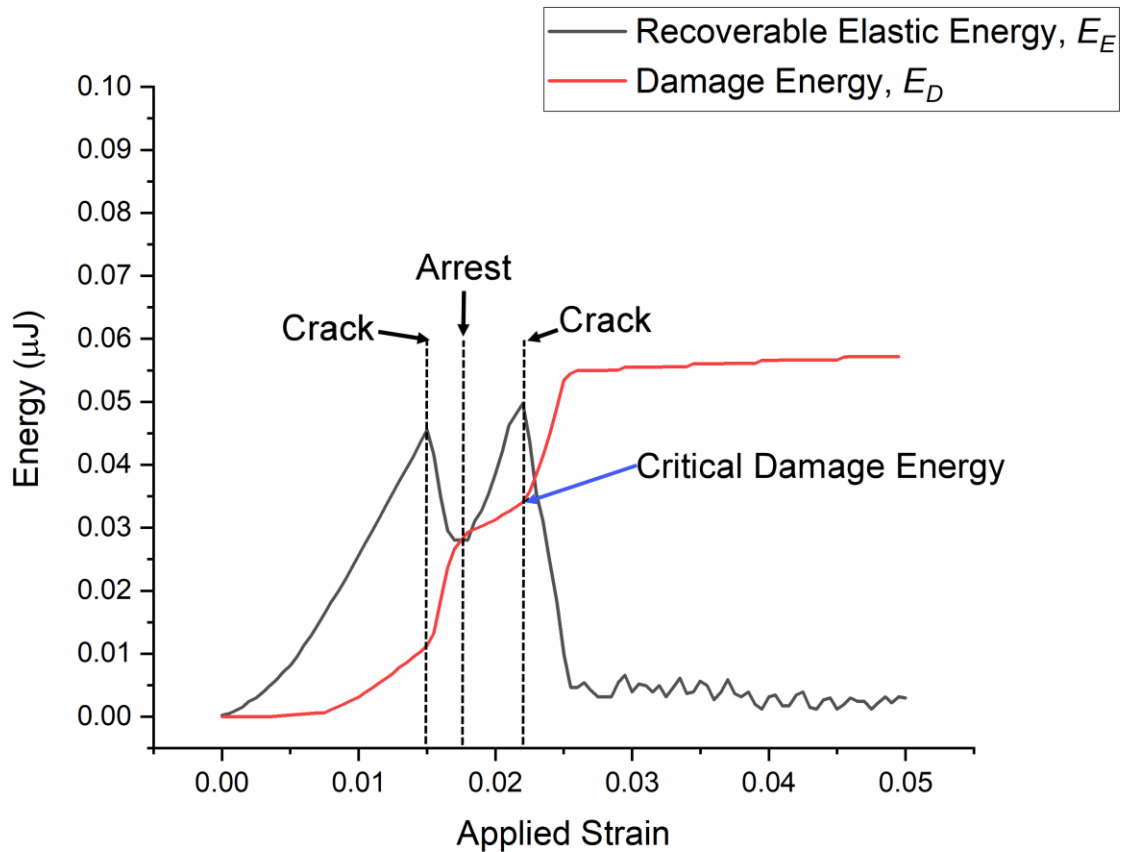
Figure 10. Change in the recoverable elastic energy and damage energy against normalised time in cases with crack arrest (Composite D in Table 1, VE size:150 μm x 90 μm, mesh size: 0.75 μm). Damage energy increases as the strain increases, with crack growth arrest. The drop of the Recoverable Elastic Energy marks the start of the fast growth of the crack.
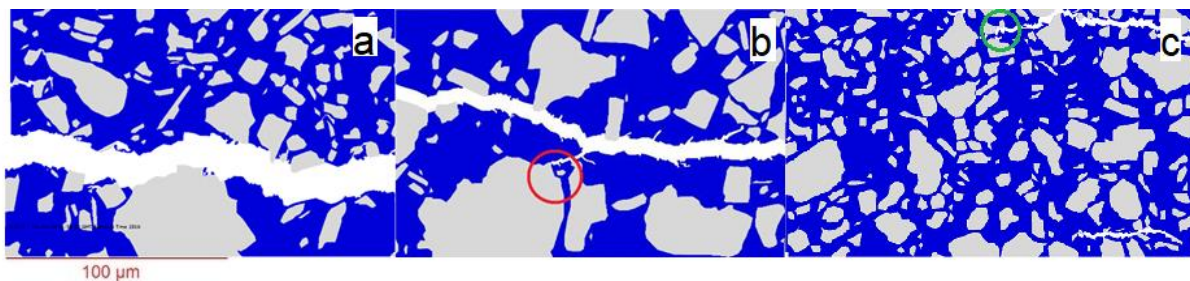

Figure 11. Typical crack growth path (a) without arrest nor agglomeration-induced matrix crack, (b) with arrest, marked by the red circle and (c) with agglomeration-induced matrix crack, marked by green circle.
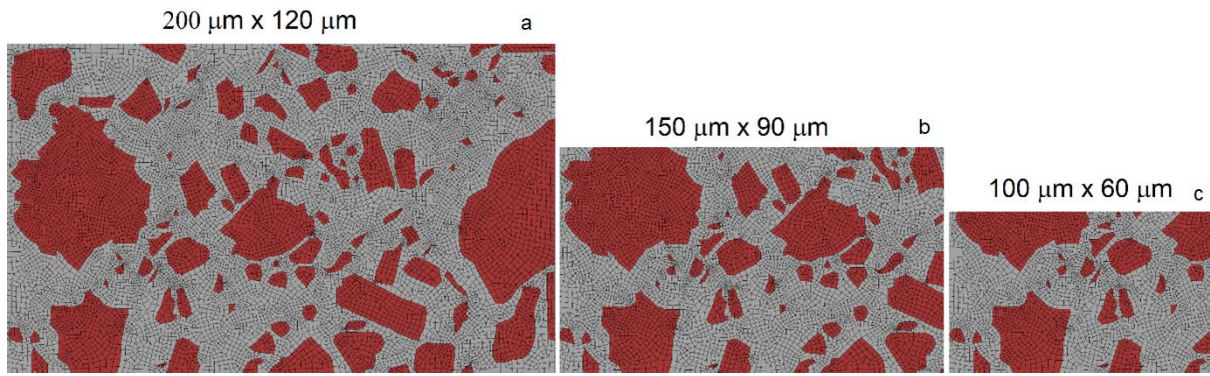
Figure 12 Typical VE used in parametric study on the effect of VE size on the FE prediction of fracture toughness (Composite C in Table 1, mesh size: 0.75 µm, a) 200 µm x 120 µm, b) 150 µm x 90 µm and c) 100 µm x 20 µm).
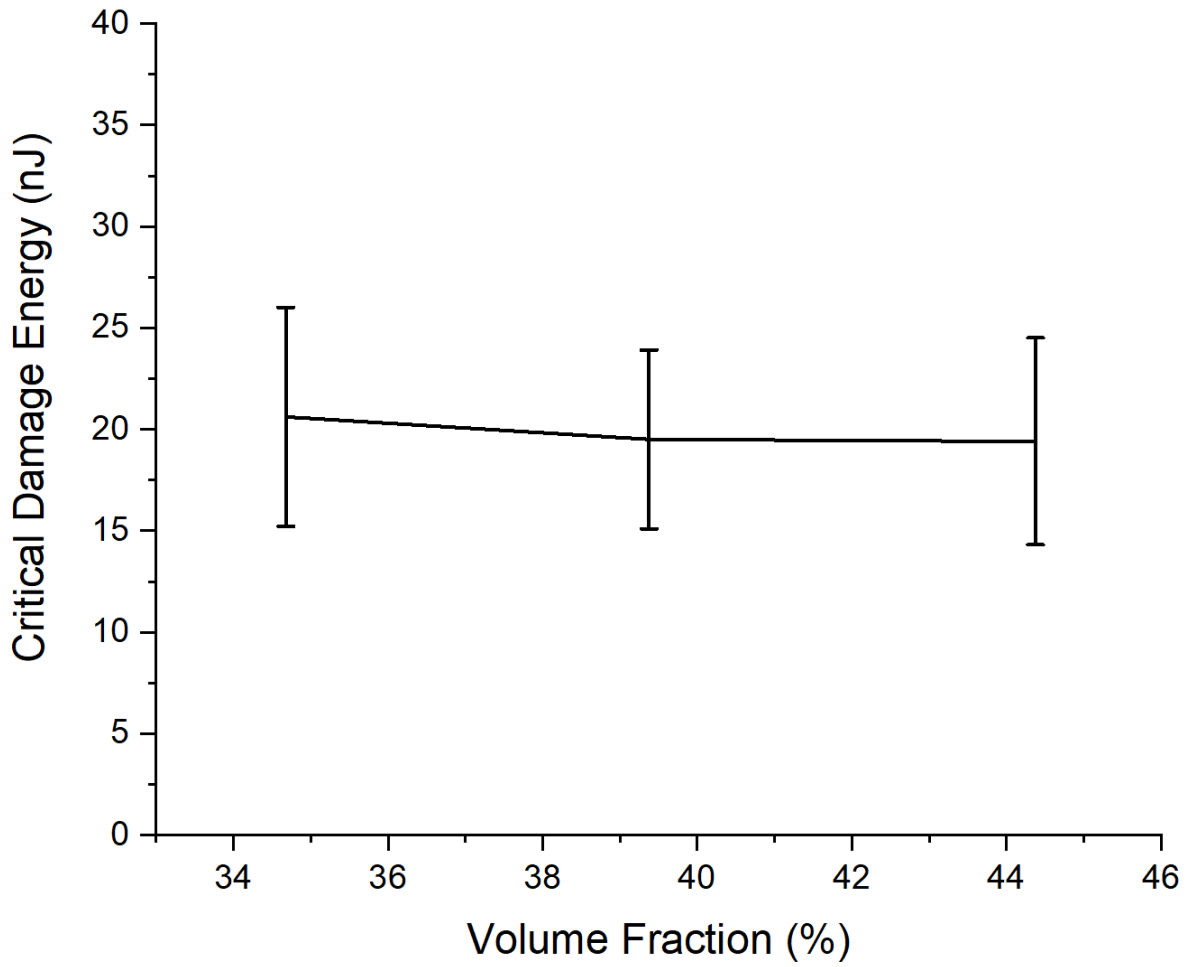
Figure 13. Critical damage energy simulation results for different volume fractions (Composites A, C and E in Table 1). The critical damage energy predicted by the FE model is almost constant as the filler content increased.
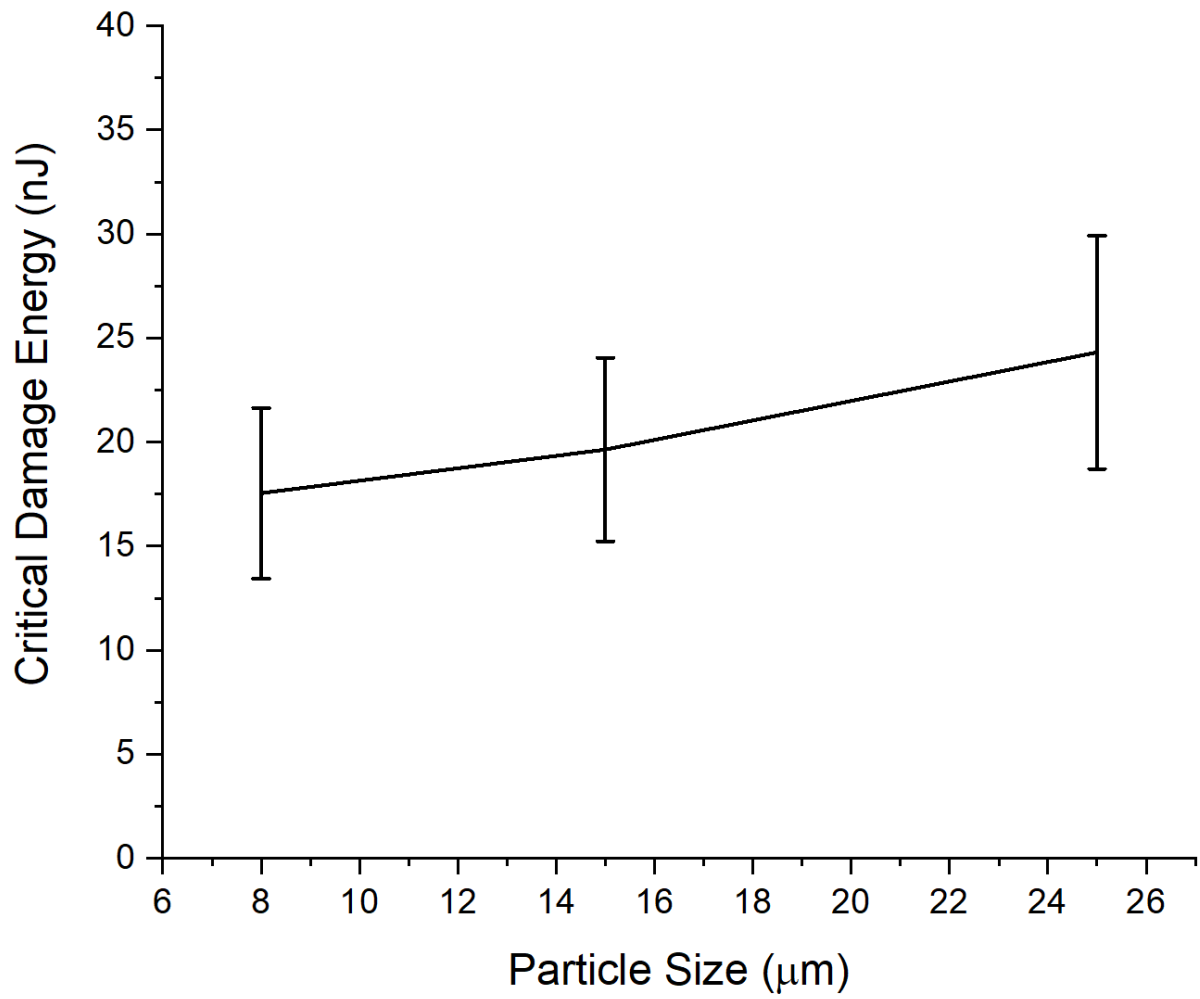
Figure 14. Critical damage energy simulation results for different mean particle diameter (Composites B, C and D in Table 1). The critical damage energy predicted by the FE model increased with increasing particle size.
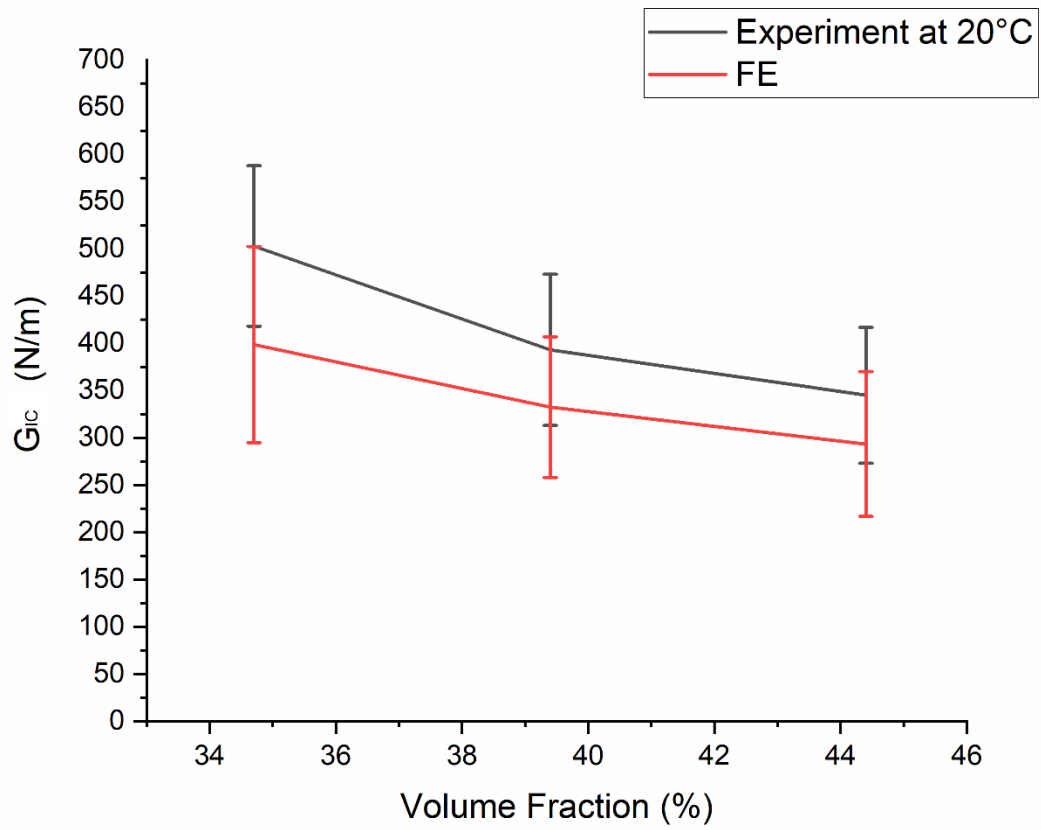
Figure 15. Effect of filler content (Composites A, C and E in Table 1) on the measured and predicted fracture toughness at 20°C. The proposed FE model gives a good estimation of the trend of the fracture toughness change with increasing filler content.
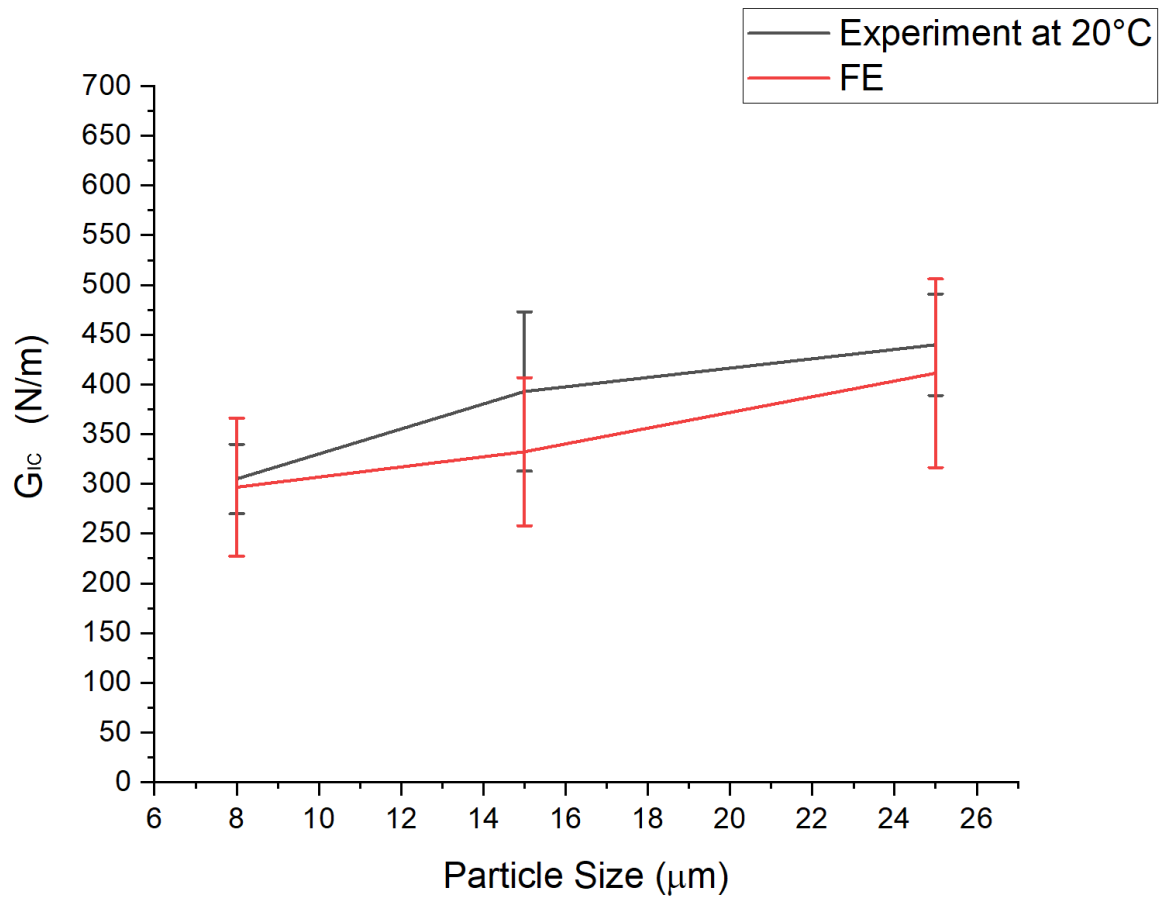
Figure 16. Effect of mean particle size (Composites B, C and D in Table 1) on the measured and predicted fracture toughness at 20°C. The proposed FE model gives a good estimation of the trend of the fracture toughness change with increasing particle size.
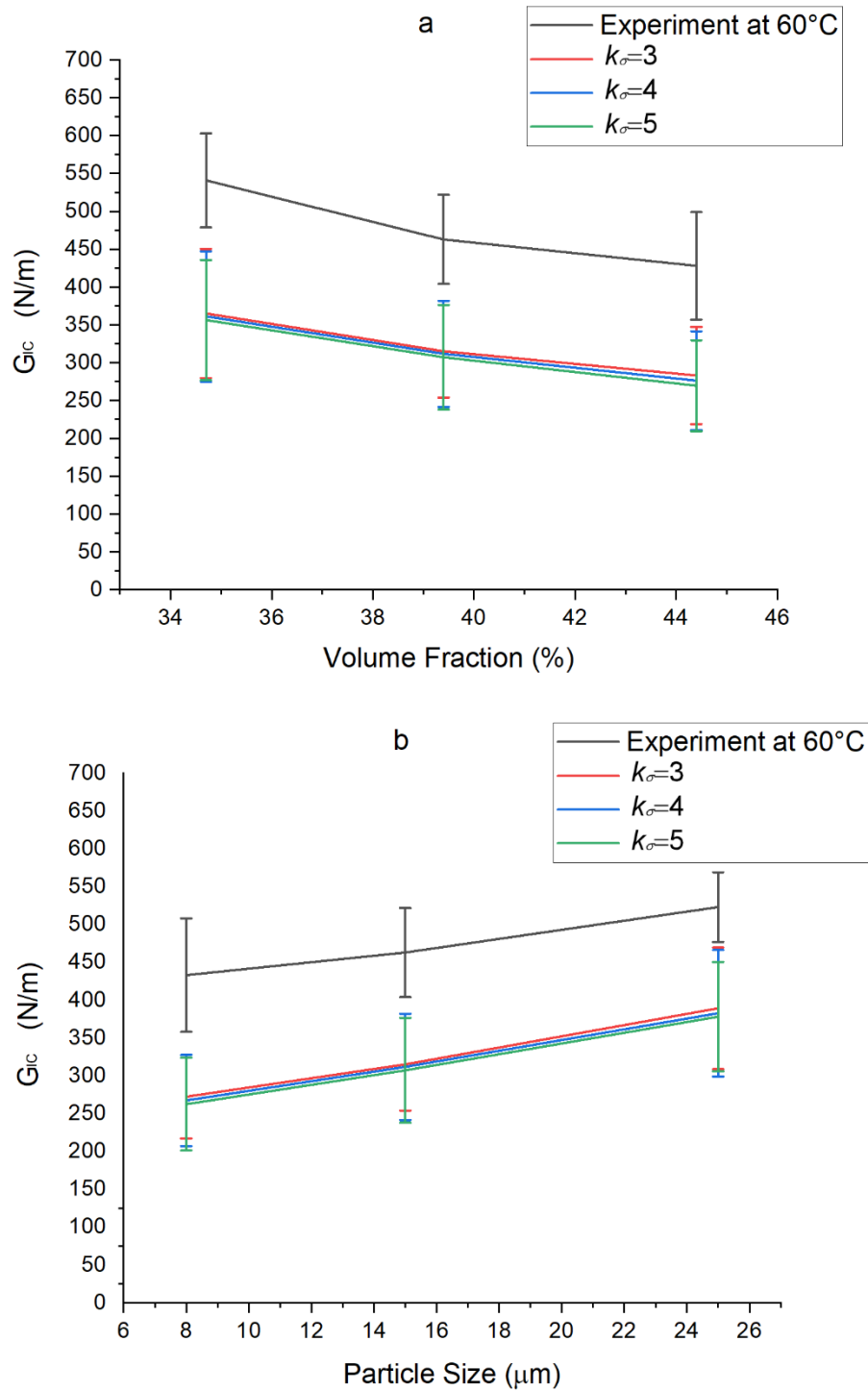
Figure 17. The effect of interfacial linear modulus, k_σ (units GPa/μm) on the fracture toughness, G_{IC}, at 60°C against (a) volume fraction (Composites A, C and E, see Table 1), and (b) particle diameter (Composites B, C and D, see Table 1). The change in k_σ shows little effect on the FE prediction of the composites' fracture toughness.
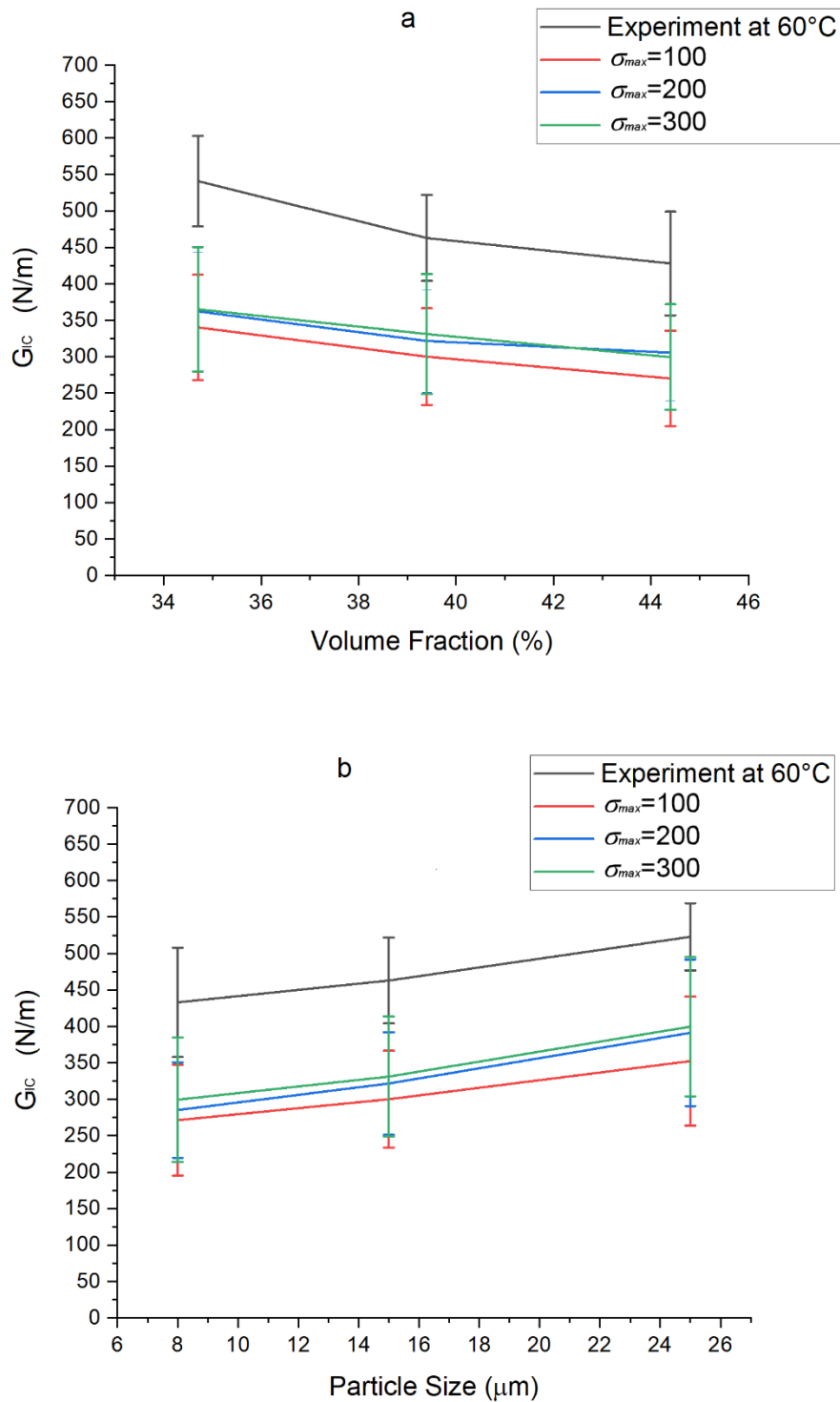
Figure 18. The effect of interfacial cohesive strength, σ_{max}^{int} (MPa) on the fracture toughness, G_{IC}, at 60°C against (a) volume fraction (Composites A, C and E, see Table 1) and (b) particle diameter (Composites B, C and D in Table 1). The increase in σ_{max}^{int} causes a minor increase in the predicted fracture toughness.
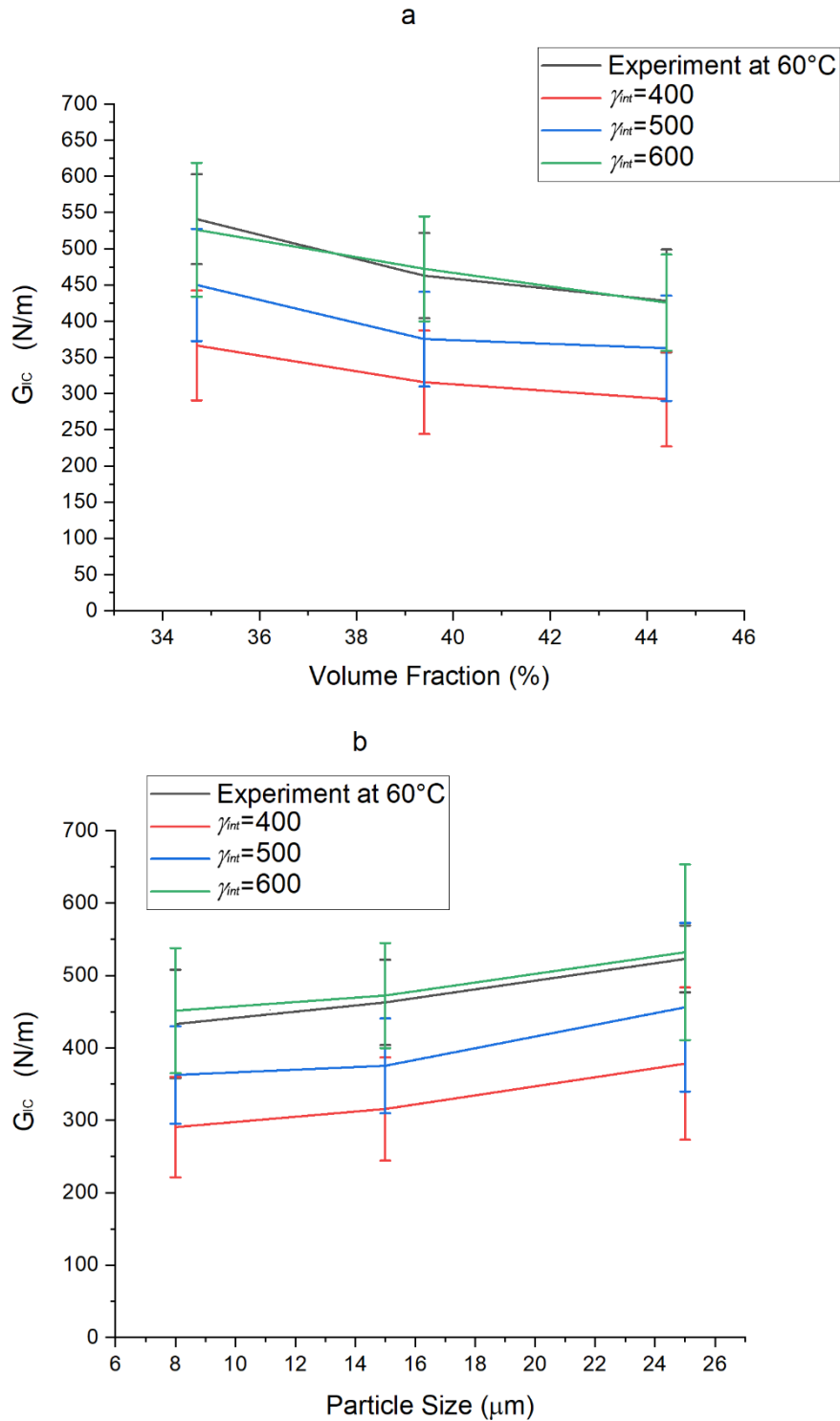
Figure 19. The effect of interfacial cohesive energy, γ_{int} (N/m), on the fracture toughness, G_{IC}, at 60°C against (a) volume fraction (Composites A, C and E, see Table 1) and (b) particle diameter (Composites B, C and D in Table 1). The change in γ_{int} affects the predicted fracture toughness significantly. When $\gamma_{int} = 600$ N/m,

the model was able to provide a good estimation of the composites' fracture toughness at 60°C.

Table 1. Particle size and volume fraction of the ATH/PMMA composites [32].

Material Code	Volume Fraction of ATH Filler (vol%)	Mean Particle Size of ATH Filler (µm)
A	34.7	15
B	39.4	8
C	39.4	15
D	39.4	25
E	44.4	15

Table 2. Material properties used as input in the FE simulations at 20°C and 60°C. Data without a reference were obtained from the experimental work of the present study; for the remaining parameters, the source of the shown values is given.

Material	Property	T = 20°C	T = 60°C
PMMA	Elastic modulus (GPa), E_m	3±0.01	2.3±0.01
	Poisson's ratio, v_m	0.38 [41]	0.39 [41]
	Fracture toughness (N/m), G_{ICm}	395±52	302±61
	Crack initiation stress (GPa)	$E_m/20$ [38]	$E_m/20$ [38]
ATH	Elastic modulus (GPa), E_f	76 [42]	76 [42]
	Poisson's ratio, v_f	0.24 [42]	0.24 [42]
ATH/PMMA interface	Interfacial linear modulus (GPa/μm), k_σ	3.61 [38]	N/A
	Interfacial cohesive strength (MPa), σ_{max}^{int}	119 [38]	N/A
	Interfacial cohesive energy (N/m), γ_{int}	430 [38]	N/A

Table 3 The FE predictions for fracture toughness obtained using VEs with different sizes (Composite C in Table 1, mesh size: 0.75 μm).

VE size	200 μm x 120 μm	150 μm x 90 μm	100 μm x 60 μm
FE predicted fracture toughness (N/m)	356±48	332±74	405±136

Table 4 The FE predictions on fracture toughness obtained using different mesh sizes (Composite C in Table 1, VE size 150 μm x 90 μm).

Mesh size	3 μm	1.5 μm	0.75 μm
FE predicted fracture toughness (N/m)	367	361	371

Table 5 The frequency of crack arresting and matrix failure-initiated crack happened in different Composites shown in Table 1 (out of fifteen simulations).

Composite ID	Crack Arrest	Agglomeration-Induced Matrix Crack
A	6/15	5/15
B	1/15	8/15
C	5/15	4/15
D	11/15	2/15
E	5/15	4/15

Table 6. Parameters used to study the effects of interfacial l interfacial linear modulus, k_σ, interfacial cohesive strength, σ_{max}^{int}, and interfacial cohesive energy, γ_{int} at 60°C.

Case			
1	$k_\sigma = 3.61 \text{ GPa/μm}$		
	$\sigma_{max}^{int} = 119 \text{ MPa}$		
	γ_{int}	400 N/m	500 N/m	600 N/m
2	$k_\sigma = 3.61 \text{ GPa/μm}$		
	$\gamma_{int} = 430 \text{ N/m}$		
	σ_{max}^{int}	100 MPa	200 MPa	300 MPa
3	$\gamma_{int} = 430 \text{ N/m}$		
	$\sigma_{max}^{int} = 119 \text{ MPa}$		
	k_σ	3 GPa/μm	4 GPa/μm	5 GPa/μm